Check for updates

Enhancing the temperature sensing property of a Ca$_{0.79-x}$Bi$_x$Er$_{0.01}$Yb$_{0.2}$MoO$_4$ phosphor *via* local symmetry distortion and reduction in non-radiative channels

Sachin Singh, Santosh Kachhap, Manisha Sharma and Sunil Kumar Singh*

We demonstrate an enhancement in the upconversion (UC) emission and temperature sensing property of a CaMoO$_4$:Er/Yb phosphor *via* distortion of the local symmetry environments and reduction in no-radiative channels. Bi^{3+} ion co-doping creates a local distortion while the average tetragonal structure of CaMoO$_4$ remains intact. This creates asymmetry around the Er^{3+} ions which improves the UC emission. Furthermore, our calculations on XRD data show a reduction in the dislocation density and the micro-strain in the crystal with the introduction of Bi^{3+}, which also favours the enhancement of UC emission as it reduces the non-radiative channels. Furthermore, the effect of this enhancement on the temperature sensing property of Er^{3+} ion has also been revealed. Our results show that the UC emission is enhanced about 25 times for Bi^{3+} co-doped samples which improves the temperature sensitivity significantly. The samples, both with and without Bi^{3+} co-doping, exhibited relative sensitivities of 0.0068 K^{-1} at 300 K and 0.0057 K^{-1} at 298 K which is a significant improvement and indicates the potential of the material for temperature sensing applications. This proof-of-concept provides a deeper understanding of the effect of Bi^{3+} doping on UC emission and opens new avenues for the development of high-performance temperature sensing materials.

1. Introduction

Optical devices rely on various optical parameters such as Rayleigh and Raman scattering, spectral transmission, radiative losses, magneto-optic methods, reflectance, and polarization-based changes, *etc.* However, as far as the temperature sensing based optical devices are concerned, they have been established mainly either through the monitoring of changes in optical emission signals, such as fluorescence intensity ratio (FIR), or through a change in fluorescence lifetime (FL) with a variation in temperature.[1] Both these techniques are unique in the sense that they are free from the source intensity. Herein, the FIR-based temperature sensing is preferred over the FL method due to its better performance. Recently, Rai *et al.* reported in detail that the FIR-based temperature sensing is better than the FL method.[2]

The FIR technique is based on the changes in emission intensity coming from a pair of thermally-coupled energy levels (TCELs) of an activator, with the typical energy gap lying in the range 200 and 2000 cm^{-1}.[3–5] Whereas, the FL based technique is related to variations in the life-time of the transitions originating from the TCELs. Among different lanthanides useful for

temperature sensing application (*e.g.* Er^{3+}, Tm^{3+}, Nd^{3+}, Eu^{3+}, and Ho^{3+}), Er^{3+} has been widely used as an activator for FIR studies[6–9] because of its suitable TCELs (^{2}H$_{11/2}$ and ^{4}S$_{3/2}$) of energy difference ($\sim$350–700 cm^{-1}).[10] However, since the quantum yield of lanthanide based upconversion emission is low, therefore, a lot of effort is still being devoted to enhance the upconversion (UC) emission at the first step and eventually enhance the sensing ability of the lanthanides thereof.

In this context, researchers have focused attentions on enhancing the efficiency of UC materials by using external and internal modifications both such as core–shell synthesis of materials, co-doping of lanthanides/non-lanthanide ions, surface plasmon resonance (SPR) based enhancement, and by alteration of the crystal structure, *etc.*[11–13] Even for a particular phase, its chemical composition, dimension of the particle (size and shape), surface morphology, site-symmetry around the activator ion, *etc.*, also play an important role in the enhancement of the UC emission intensity.[14–22] Particularly, the site symmetry of Ln^{3+} doped phosphors may critically affect the UC/DS luminescence as the electronic energy levels and excited-state dynamics of the doped Ln^{3+} ions may change significantly with a slight change in the local site symmetry.[23–25]

Ln^{3+}-doped disordered crystals (such as molybdates, fluorides, tungstates, garnets, *etc.*) are most common examples for

Department of Physics, Indian Institute of Technology (Banaras Hindu University), Varanasi-221005, India. E-mail: sunilks.app@iitbhu.ac.in

the breakdown of crystallographic site symmetry under doping of non-lanthanide ions.[26,27] Their luminescence properties have been improved by co-doping with specific ions.[28–32] For example, Wisser *et al.* introduced the local symmetry distortion in Er/Yb: $NaYF_4$ nanocrystals (*via* substituting Gd^{3+} and Lu^{3+} at Y^{3+}) which leads to an increase in radiative transition rates of Er^{3+} ions.[33] Similarly, Zhu *et al.* observed the synergistic effect of the doping of trace alkali metal ions (Li^+, K^+, Na^+) in K_2LiAlF_6:-Mn^{4+}.[34] Wang *et al.* also studied the effect of site symmetry for the Eu^{3+} ions doped in $NaLu(WO_4)_2$. Wang *et al.* reported that the doping of Sc^{3+} in $Er^{3+}/Yb^{3+}:Y_2O_3$ manipulates the lattice site symmetry and enhances the radiative emission of Er^{3+}.[35]

Similarly, there are numerous reports for creating local site symmetry distortion using Bi^{3+} ion as co-dopant also.[36,37] Bi^{3+} ion was used as a co-dopant to create local site symmetry distortion in the $Y_2O_3:Eu^{3+}$ phosphor, resulting in enhanced luminescence properties. The authors attributed this enhancement to the increased crystal field splitting and improved energy transfer efficiency between Eu^{3+} and Bi^{3+} ions.[36] Xue *et al.* investigated the effect of Bi^{3+} ion co-doping on the photoluminescence and thermal stability of perovskite-type $CsPbBr_3$ nanocrystals. The authors found that the Bi^{3+} ion co-doping enhanced the luminescence properties of the nanocrystals and improved their thermal stability by reducing the defect density and passivating the surface traps. The results suggest the potential use of Bi^{3+} ion co-doping as a strategy to improve the stability and performance of perovskite-type nanocrystals for optoelectronic applications.[37]

Considering above research findings and with the aim of enhancing the luminescence intensity and temperature sensing property of Er^{3+} ions, this paper explores the co-doping of Bi^{3+} in $Er^{3+}/Yb^{3+}:CaMoO_4$ phosphor. We have analyzed the site symmetry and optical properties of two samples in detail, one without Bi^{3+} co-doping ($Ca_{0.79}Er_{0.01}Yb_{0.2}MoO_4$) and the other with optimized Bi^{3+} co-doping ($Ca_{0.68}Bi_{0.11}Er_{0.01}Yb_{0.2}MoO_4$). Our results show that the UC emission intensity is enhanced about 25 times which improves the temperature sensitivity significantly. Conclusively, the study provides insight into the potential of Bi^{3+} co-doping for improving the performance of Er^{3+}/Yb^{3+} co-doped $CaMoO_4$ as a temperature sensor in FIR based applications.

2. Materials and methods

2.1 Materials

To introduce Ca^{2+} ions, calcium oxide (CaO) (Alfa Aesar, 97%) was utilized, while ammonium molybdate ((NH_4)$_6$-$Mo_7O_{24} \cdot 4H_2O$, 99.0%) (AR) served as sources of Mo^{6+} ions. Urea (NH_2CONH_2) (Fisher Scientific) was used as a fuel. The dopant ions Er^{3+}, Bi^{3+}, and Yb^{3+} were introduced through the use of erbium(III) oxide (Er_2O_3, 99.9%, REO, Alfa Aesar), bismuth(III) oxide (Bi_2O_3, 99.99%, REO, Alfa Aesar), and ytterbium(III) oxide (Yb_2O_3, 99.99%, REO, Alfa Aesar), respectively. To make the nitrate solution of the precursors, nitric acid (HNO_3, 69%, Merck) is used. Cleaning was carried out using propane-2-ol ((CH_3)$_2CHOH$, 99.0%, Thermo Fisher Scientific), and acetone

(CH_3COCH_3, 99.0%, Merck), while double-distilled water was utilized as an intermediate additive.

2.2 Synthesis

The gel-combustion method was utilized to synthesize the series of stoichiometric $Ca_{0.79-x}Bi_xEr_{0.01}Yb_{0.2}MoO_4$ ($x = 0.00$, 0.02, 0.05, 0.08, 0.11, and 0.14) phosphors.[10] For the synthesis of $Ca_{0.79}Er_{0.01}Yb_{0.2}MoO_4$, 3.5 mmol of CaO precursor was placed in a beaker, and required amount of nitric acid was added to it drop-wise with continuous stirring of 200 rpm on a hot plate maintained at 100 °C until a transparent nitrate solution was obtained. The nitrate solution of Er_2O_3, and Yb_2O_3 are formed by the similar steps by taking the amount, respectively of 0.02 mmol and 0.44 mmol in HNO_3. In a separate beaker, 0.63 mmol of (NH_4)$_6Mo_7O_{24} \cdot 4H_2O$ was dissolved in 30 ml DI water at 30 °C. 1.5 mg of urea that act as a fuel in combustion reaction was added into it, and the temperature was raised to 100 °C. Then, all the individually prepared solutions were mixed in a beaker and kept on a hot plate maintained at 210 °C with continuous stirring of 200 rpm until the solution became gel-like. Then, the temperature of the solution was raised to 450 °C, for the combustion reaction. Within 1 minute, auto-ignition took place, resulting a foam-like porous product. The series of Bi-doped $Ca_{0.79-x}Bi_xEr_{0.01}Yb_{0.2}MoO_4$ ($x = 0.02$, 0.05, 0.08, 0.11, and 0.14) samples were obtained by taking additional required molar amount of Bi_2O_3 following the above-mentioned steps. The final foam-like product of all the series is then ground using agate mortar to obtain a powder for further characterizations. The samples are further calcined at 900 °C for improving the optical behaviour.

2.3 Characterization techniques

The study utilized various techniques to analyse the powder samples, including X-ray diffraction (XRD) using a Rigaku-MiniFlex-II DESKTOP X-ray diffractometer with a Cu-Kα radiation source at 30 kV and 15 mA, infrared (IR) spectroscopy using a FT/IR 4600 spectrophotometer (JASCO) at room temperature, field-emission scanning electron microscopy (FE-SEM) (Nova Nano SEM 450, USA) to determine particle size and surface morphology, photoluminescence spectroscopy using a Fluorolog-3 spectrophotometer (HORIBA Jobin Yvon), and temperature-dependent UC emission measurements using a handmade heater with a k-type thermocouple and a continuous-wave (CW) 980 nm tunable power diode laser (model: ADR 1805, class IV) with a maximum power of 2 W. Samples CMEY ($Ca_{0.79}Er_{0.01}$-$Yb_{0.2}MoO_4$) and CMBEY ($Ca_{0.68}Bi_{0.11}Er_{0.01}Yb_{0.2}MoO_4$) were used for the comparative studies of various properties. The operating laser power and integration time of spectrometer during the scan from 500 to 575 nm were kept low at 24 mW and 10 ms, respectively to minimize laser-induced heating effects.

3. Results and discussion

3.1 X-ray diffraction measurement

3.1.1 Phase and structure analysis. X-ray diffraction (XRD) analysis was conducted to study the structure and phase of the

synthesized $Ca_{0.79-x}Bi_xEr_{0.01}Yb_{0.2}MoO_4$ ($x = 0.00, 0.02, 0.05, 0.08, 0.11,$ and 0.14) phosphor. The resulting XRD patterns of the $Ca_{0.79-x}Bi_xEr_{0.01}Yb_{0.2}MoO_4$ ($x = 0.00, 0.02, 0.05, 0.08, 0.11,$ and 0.14) are presented in Fig. 1(a). The most prominent diffraction peaks were observed at 2θ angles of $18.73, 28.86, 31.44, 34.42, 47.31, 49.47, 54.41, 58.29, 59.80,$ and $76.60°$. The highest intensity peak centered at 2θ angle $28.86°$ was monitored closely to observe the peak shift in the diffraction pattern with the Bi-doping, as shown in Fig. 1(b). It was observed that the peak shifts towards higher angles with increasing Bi content from $x = 0.02$ to 0.08 in $Ca_{0.79-x}Bi_xEr_{0.01}Yb_{0.2}MoO_4$. With further increase in the amount of Bi, the peak shifts towards the lower angle side. Initially, the Bi atom successfully occupies the Ca-lattice site. However, beyond the doping amount $x = 0.08$, the Bi atoms take the interstitial site, resulting in peak shift towards the lower angle. However, the diffraction peak shift is very small. The shift in the diffraction peak can also be attributed to the difference in ionic radii between Ca^{2+} and Bi^{3+} ions, as Bi^{3+} has a larger ionic radius than Ca^{2+}. When Bi^{3+} ions replace Ca^{2+} ions in the crystal lattice, it leads to an expansion of the unit cell, resulting in a slight distortion of the local environment around the substituted sites which is explained in detail in the XRD-refinement data analysis in the following section. However, the peak shift points to the successful incorporation of Bi^{3+} ions into the $CaMoO_4$ lattice structure and the subsequent distortion of the local symmetry environments. Notably, no significant peak changes or evolution of the new phase of $CaMoO_4$ were observed in this series, which confirms the stability of the parent structure and phase of the synthesized samples. However, a progressive evolution of h-MoO_3 is observed which has been marked with astrix.[38]

The Debye–Scherrer formula was used to find the average crystallite size of $Ca_{0.79}Er_{0.01}Yb_{0.2}MoO_4$ and $Ca_{0.68}Bi_{0.11}Er_{0.01}Yb_{0.2}MoO_4$ samples, given in eqn (1).

$$D = \frac{0.89\lambda}{\beta \cos\theta} \quad (1)$$

where, D is the crystallite size, λ is the wavelength of the X-ray source, β is the full width half maximum, and θ is the Bragg angle of diffraction. The calculated value of average crystallite size of $Ca_{0.79}Er_{0.01}Yb_{0.2}MoO_4$ and $Ca_{0.68}Bi_{0.11}Er_{0.01}Yb_{0.2}MoO_4$ phosphors are 117.2 nm and 140.0 nm, respectively. This increment in crystallite size confirms the improvement in the crystallinity of sample without altering any noticeable change in the phase after the doping of Bi ion.[39] Further, to observe the effect of Bi doping on the crystallographic defects or irregularity, the dislocation density of $Ca_{0.79}Er_{0.01}Yb_{0.2}MoO_4$ and $Ca_{0.68}Bi_{0.11}Er_{0.01}Yb_{0.2}MoO_4$ phosphors were calculated by using the following relation:

$$\delta = \frac{1}{D^2} \quad (2)$$

where, δ is the dislocation density and D is the crystallite size. The dislocation density calculated for $Ca_{0.79}Er_{0.01}Yb_{0.2}MoO_4$ phosphor is 72.80×10^{12} m^{-2}. Whereas the dislocation density decreases after the doping of Bi and it is found to be 51.02×10^{12} m^{-2}. Thus, the doping of Bi reduces the number of dislocations in the crystal structure and thus expected to reduce the probability of non-radiative losses from lanthanide ions.[39]

Similarly, the effect of Bi doping on the distortion of lattice structure was also calculated by using the following relation;

$$e = \frac{\beta}{4 \tan\theta} \quad (3)$$

where, e is the macrostrain, β is the FWHM, and θ is the diffraction angle. The micro-strain thus calculated is 16.8×10^{-4} and 15.8×10^{-4} for $Ca_{0.79}Er_{0.01}Yb_{0.2}MoO_4$ and $Ca_{0.68}Bi_{0.11}Er_{0.01}Yb_{0.2}MoO_4$ phosphors, respectively. The reduction in the dislocation density and micro-strain with the introduction
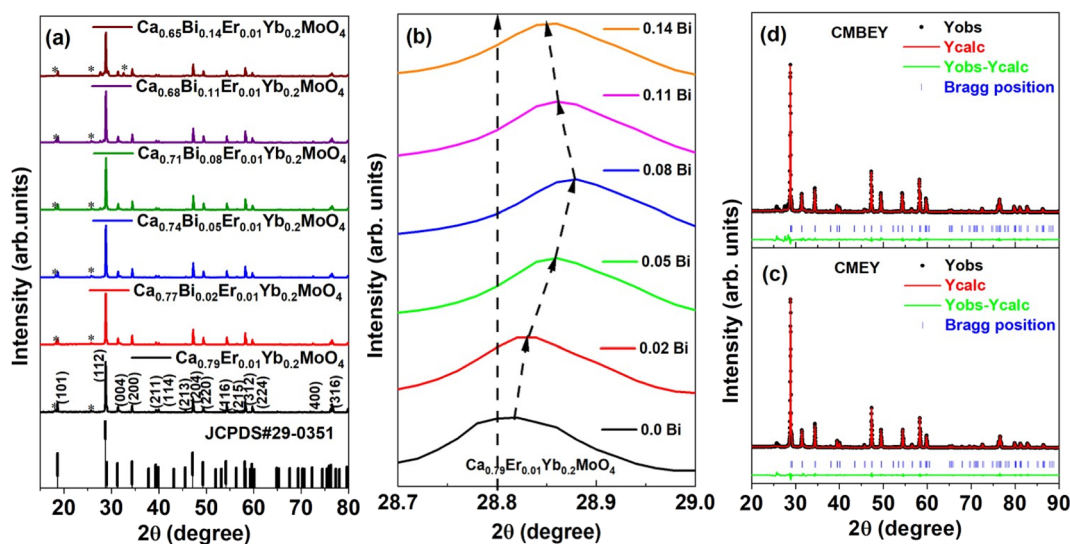

Fig. 1 (a) XRD patterns of $Ca_{0.79-x}Bi_xEr_{0.01}Yb_{0.2}MoO_4$ ($x = 0.00, 0.02, 0.05, 0.08, 0.11,$ and 0.14) powder samples. (b) Expanded XRD patterns of $Ca_{0.79-x}Bi_xEr_{0.01}Yb_{0.2}MoO_4$ ($x = 0.0, 0.02, 0.05, 0.08, 0.11,$ and 0.14) powder samples between 2θ angle 28.7 to $29.0°$. Rietveld refined XRD patterns of (c) $Ca_{0.79}Er_{0.01}Yb_{0.2}MoO_4$, and (d) $Ca_{0.68}Bi_{0.11}Er_{0.01}Yb_{0.2}MoO_4$ powder samples.

of Bi in $Ca_{0.79}Er_{0.01}Yb_{0.2}MoO_4$ crystal favours the enhancement of upconversion emission intensity.

3.1.2 Rietveld refinement analysis. The determination of the structural parameter and the phase of the synthesized $Ca_{0.79}Er_{0.01}Yb_{0.2}MoO_4$ and $Ca_{0.68}Bi_{0.11}Er_{0.01}Yb_{0.2}MoO_4$ powder samples were carried out using Rietveld refinement using the FullProf software. A linear interpolation function with refinable heights was selected as the background function, and the Pseudo-Voigt peak shape function was chosen to perfectly fit the diffraction peaks of the XRD pattern. Fig. 1(c) and (d) show the Rietveld refined XRD patterns of the $Ca_{0.79}Er_{0.01}Yb_{0.2}MoO_4$ and $Ca_{0.68}Bi_{0.11}Er_{0.01}Yb_{0.2}MoO_4$ powder samples, respectively, while Table 1 summarizes the lattice parameters and various fitted parameters.

The results of the Rietveld refinement show that the structure and phase of the undoped and Bi-doped $Ca_{0.68}Bi_{0.11}Er_{0.01}Yb_{0.2}MoO_4$ are the same. The lattice parameters of the $Ca_{0.79}Er_{0.01}Yb_{0.2}MoO_4$ powder sample are $a = b = 5.206(59)$ Å, $c = 11.368(93)$ Å, $\alpha = \beta = \gamma = 90°$. The volume of the structure is $308.19(6)$ Å^3, and the density obtained is 6.878 g cm^{-3}. In contrast, the lattice parameters are increased in the Bi-doped optimized $Ca_{0.68}Bi_{0.11}Er_{0.01}Yb_{0.2}MoO_4$ powder sample, with $a = b = 5.211(65)$ Å and $c = 11.389(72)$ Å. This is in good agreement with the doping of a higher ionic radius Bi-ion in place of the Ca-site. The doping of Bi-ion increases the volume of the structure and lowers the density compared to the undoped one. The volume and density are $309.35(9)$ Å^3, and 6.562 g cm^{-3}, respectively. The coordination number of Ca-atom is 8, bonded with the neighbouring O-atoms, and form CaO_8 polyhedra unit. Mo-atom shows coordination number 4 with nearby four O-atoms and results the formation of MoO_4 tetrahedral structure. In CaO_8 unit, four different bond lengths of the Mo-atom with O-atoms are present, and in MoO_4 unit, only one type of bond length of Ca-atom with O-atoms is present (as indicated in Fig. 2(a) and (b)). There bonds of the $Ca_{0.79}Er_{0.01}Yb_{0.2}MoO_4$ and Bi-doped $Ca_{0.68}Bi_{0.11}Er_{0.01}Yb_{0.2}MoO_4$ tetragonal structure with space group $I4_1/a$ are listed in Table 2.[10] Similarly, some of the bond angles formed among the Ca, Mo, and O-atoms are also summarized in Table 2.

The increased lattice parameter in optimized $Ca_{0.68}Bi_{0.11}Er_{0.01}Yb_{0.2}MoO_4$ is also observed by the bond length and

bonding angle, with larger bond lengths (except M–O bonds) and Ca–O–Ca bonding angle shrinking compared to the undoped sample. In contrast, the Ca–O–Mo bonding angle increases, in agreement with the increased lattice parameters of the crystal structure in Bi-doped $Ca_{0.68}Bi_{0.11}Er_{0.01}Yb_{0.2}MoO_4$. Thus, the Bi^{3+} ions incorporation at the Ca^{2+} ions site in the crystal lattice expands the unit cell. The expansion of the crystal structure is observed by the bond length and bond angle change in the Bi^{3+} doped sample also, obtained by the Rietveld refinement. These changes result a slight distortion of the local environment around the substituted sites where lanthanides are also doped. The CaO_8 polyhedral unit distortion (D) in the crystal structure of $Ca_{0.79}Er_{0.01}Yb_{0.2}MoO_4$ and $Ca_{0.68}Bi_{0.11}Er_{0.01}Yb_{0.2}MoO_4$ are calculated using the following equation.[41]

$$D = \frac{1}{n}\left[\sum_i^n \left(\frac{d_i - d}{d}\right)^2\right] \qquad (4)$$

where, n is the coordination number (for CaO_8 polyhedra $n = 8$), d_i and d, respectively, are the individual and average distance of the O-atoms from the central Ca-atom in the polyhedra unit obtained after Rietveld refinement. The calculated D values for the polyhedral units in $Ca_{0.79}Er_{0.01}Yb_{0.2}MoO_4$ and $Ca_{0.68}Bi_{0.11}Er_{0.01}Yb_{0.2}MoO_4$ are 6.36×10^{-5} and 7.28×10^{-5}, respectively. Hence, the bond length related CaO_8 polyhedral distortion in $Ca_{0.68}Bi_{0.11}Er_{0.01}Yb_{0.2}MoO_4$ is more than the $Ca_{0.79}Er_{0.01}Yb_{0.2}MoO_4$. This may be the one of the reasons of increased luminescence intensity in the Bi^{3+}-doped sample as compared to undoped one. The local site distortion can influence the luminescent properties of the lanthanide doped phosphors, as it can alter the energy levels via crystal field splitting and local coordination environment of Er^{3+}/Yb^{3+} ions.

3.2 SEM and EDS measurements: surface morphology and elemental analysis

The surface morphologies of $Ca_{0.79}Er_{0.01}Yb_{0.2}MoO_4$ (CMEY) and $Ca_{0.68}Bi_{0.11}Er_{0.01}Yb_{0.2}MoO_4$ (CMBEY) samples annealed at 900 °C were analysed using field emission scanning electron microscopy (FESEM) as shown in Fig. 3(a) and (b). Images illustrate the presence of irregular and non-uniform aggregated particles, with the average particle size of about 1.982 μm and 3.230 μm, respectively for CMEY and CMBEY

Table 1 Rietveld refined structure parameters of the $Ca_{0.79}Er_{0.01}Yb_{0.2}MoO_4$ and $Ca_{0.68}Bi_{0.11}Er_{0.01}Yb_{0.2}MoO_4$ powder samples

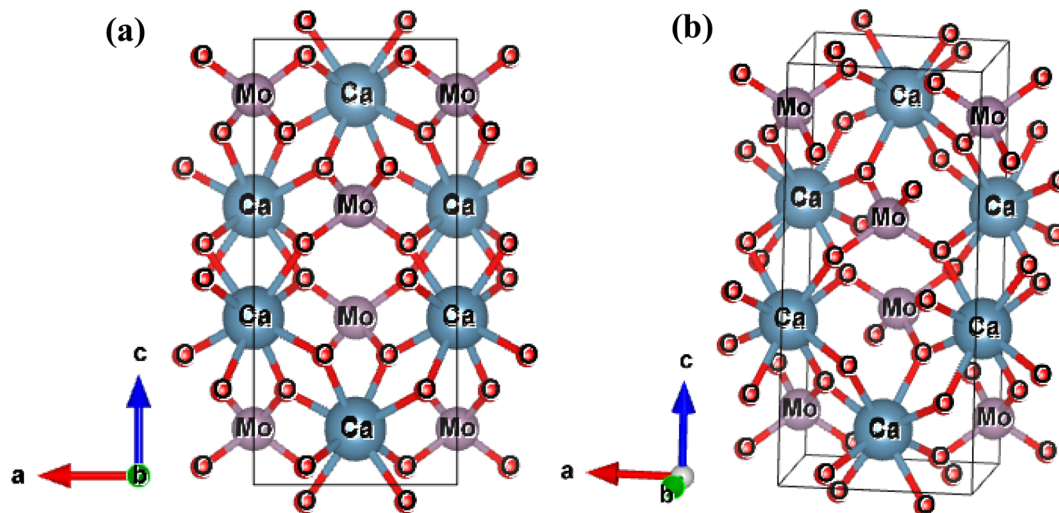| Structure parameter	$Ca_{0.79}Er_{0.01}Yb_{0.2}MoO_4$	$Ca_{0.68}Bi_{0.11}Er_{0.01}Yb_{0.2}MoO_4$
Structure	Tetragonal	Tetragonal
Space group	$I4_1/a$ (88)	$I4_1/a$ (88)
$a = b$ (Å)	5.20659 ± 0.00004	5.21165 ± 0.00004
c (Å)	11.36893 ± 0.00014	11.38972 ± 0.00019
$\alpha = \beta = \gamma$ (°)	90	90
Volume (Å^3)	308.196 ± 0.005	309.359 ± 0.006
Density (g cm^{-3})	6.878	6.562
R_p	4.47	5.56
R_{wp}	7.27	9.15
R_{exp}	2.24	2.41
χ^2	10.5	14.4

Fig. 2 Tetragonal crystal structure of $Ca_{0.79}Er_{0.01}Yb_{0.2}MoO_4$ in two different orientation obtained after Rietveld refinement of the XRD patterns.

samples. The increase in particle size is attributed to Bi^{3+} doping.[40] The spherical particles of the phosphor were found to agglomerate in different orientations which is the characteristic property with combustion synthesized oxide phosphors.[8–10]

Energy dispersive X-ray spectroscopy (EDS) patterns of CMEY and CMBEY phosphor samples were also obtained. The EDS spectrum of CMBEY, shown in Fig. 3(d), confirms the presence of Ca, Mo, Er, Yb, O, and Bi elements, while CMEY phosphor contains Ca, Yb, Er, O, and Mo elements only, as shown in Fig. 3(c).[10] The addition of Bi^{3+} ion in the co-doped phosphor was thus confirmed by the presence of an additional Bi element along with Ca, Er, Yb, O, and Mo elements in CMBEY phosphor, as shown in Fig. 3(d). The successful doping of Er^{3+}, Yb^{3+}, and Bi^{3+} in the $CaMoO_4$ host was also verified by the elemental analysis of Er, Yb, Ca, Mo, O, and Bi.

3.3 Optical properties

3.3.1 FTIR and UV-vis absorption measurement analysis. Fig. 4(a) exhibits the Fourier transform infrared (FTIR) spectra of CMEY and CMBEY in transmittance mode, spanning from wavenumber 400 cm^{-1} to 4000 cm^{-1}. In a free space environment, the $(MoO_4)_2$ tetrahedrons of $CaMoO_4$ display T_d-symmetry,[42,43] which means they are symmetric with respect to a group of four symmetry operations: rotation by $360°/n$ (where n is the number of symmetry elements), reflection through a plane perpendicular to a symmetry axis, and inversion through a point. However, when the $(MoO_4)_2$ tetrahedrons are incorporated into the lattice of $CaMoO_4$, the symmetry is reduced to S_4, which means there is only a four-fold rotational axis of symmetry. This reduction in symmetry can be caused by the distortion of the local environment around the $(MoO_4)_2$ tetrahedrons due to interactions with the surrounding atoms in

Table 2 The bond length and angle in Ca, Mo and O-atoms obtained after the Rietveld refinement of the XRD patterns of $Ca_{0.79}Er_{0.01}Yb_{0.2}MoO_4$ and $Ca_{0.68}Bi_{0.11}Er_{0.01}Yb_{0.2}MoO_4$ powder samples

	$Ca_{0.79}Er_{0.01}Yb_{0.2}MoO_4$	$Ca_{0.68}Bi_{0.11}Er_{0.01}Yb_{0.2}MoO_4$
Bonding atoms	Bond length (Å)	Bond length (Å)
Ca1–O1, O5	2.39086(0)	2.39902(0)
Ca1–O2, O6	2.41854(0)	2.42656(0)
Ca1–O3, O7	2.38182(3)	2.38770(3)
Ca1–O4, O8	2.43470(3)	2.44077(3)
Mo–O1, O9, O10, O11	1.83473(0)	1.82896(0)
Bonding atoms	**Bond angle (°)**	**Bond angle (°)**
Ca1–O1–Ca3	107.1402(5)	105.7841(5)
Ca1–O8–Ca3	107.1402(5)	106.5917(5)
Ca1–O6–Ca2	106.8159(5)	105.7841(5)
Ca1–O7–Ca2	105.7055(5)	106.9151(5)
Ca1–O1–Mo1	120.6542(8)	120.7090(8)
Ca1–O7–Mo2	130.0464(4)	130.3818(4)
Mo1–O1–Ca3	130.1155(4)	130.3818(4)
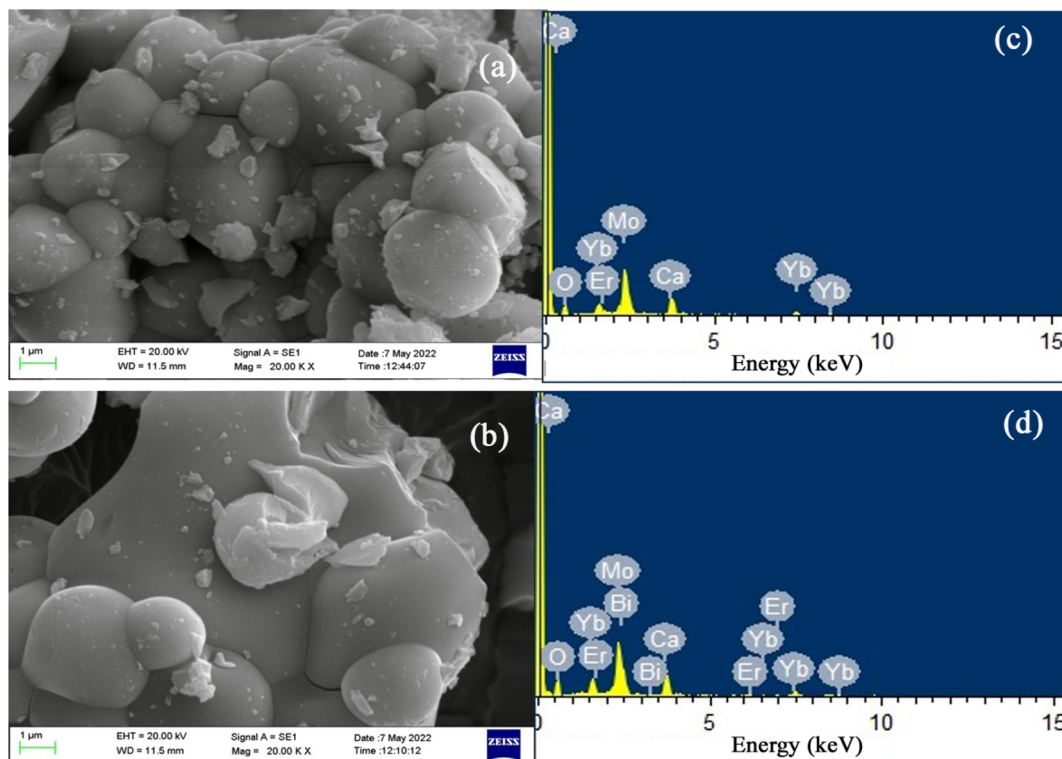
Fig. 3 SEM image of (a) $Ca_{0.79}Er_{0.01}Yb_{0.2}MoO_4$ (CMEY) and (b) $Ca_{0.68}Bi_{0.11}Er_{0.01}Yb_{0.2}MoO_4$ (CMBEY) phosphors. The EDS spectra of (c) CMEY (d) CMBEY phosphors.

the lattice. The bending vibration of H–O–H is indicated by the peaks observed at 1608 cm^{-1}, while the stretching vibration of O–H groups is evidenced by the peak observed at 3451 cm^{-1}.[10,44] A minor peak observed at 2347 cm^{-1} specifies the stretching vibration of the C–H group.[45] The fingerprint region is characterized by two prominent vibrational bands of the $[MoO_4]_2$. The first one, centred at $\sim$433 cm^{-1}, is due to the bending of Mo–O bonds,[46] while the second one, centred at 790 cm^{-1}, results from the asymmetric stretching vibration of the O–Mo–O bond.[10] Fig. 4(a) demonstrates a notable decrease in the intensity of O–H band at 3451 cm^{-1} in the presence of Bi^{3+} ions.[40] This observation supports the notion that increasing the doping concentrations of Bi^{3+} ions has the potential to increase the emission intensity arising from the thermally coupled levels of Er^{3+} ion.

Fig. 4(b) and (c) depicts the optical absorption of both the CMEY and CMBEY samples, providing valuable insights into the bandgap properties of the samples. The broad absorption band observed in both CMEY and CMBEY samples at a center point of 300 nm is attributed to charge transfer from O$_2$-(2p) electrons to Mo^{6+} bands.[47] The bandgap energy of the samples is determined from the Tauc plots given in insets of the corresponding absorption spectra. The bandgap energy of CMEY sample is 3.64 eV, while it reduces to 3.20 eV for CMBEY sample. The variations in the energy band gap values observed in the doped and undoped phosphors could be attributed to the diverse crystalline morphology and size of the material, stemming from the distinct lanthanide ions used. Further, the presence of the Bi^{3+}, Er^{3+}, and Yb^{3+} ions create defects in the CaMoO$_4$ material, generating supplementary energy levels in
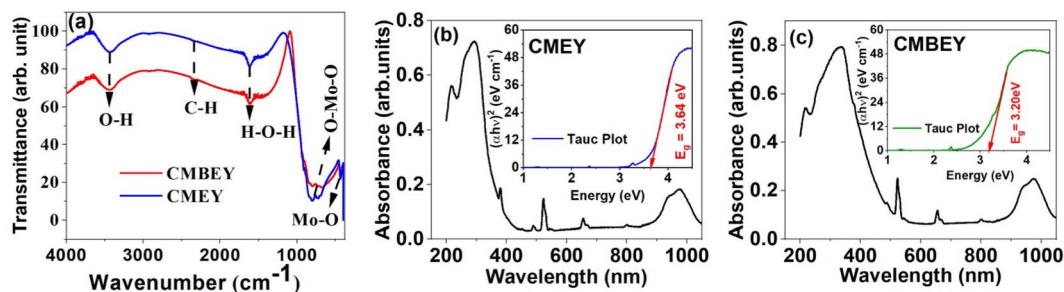

Fig. 4 (a) Fourier transform infrared spectra of CMEY and CMBEY samples. UV-Vis-NIR absorption spectrum of (b) CMEY, and (c) CMBEY phosphors. Tauc plots of the respective UV-visible absorption spectra are provided as insets of the corresponding figures.
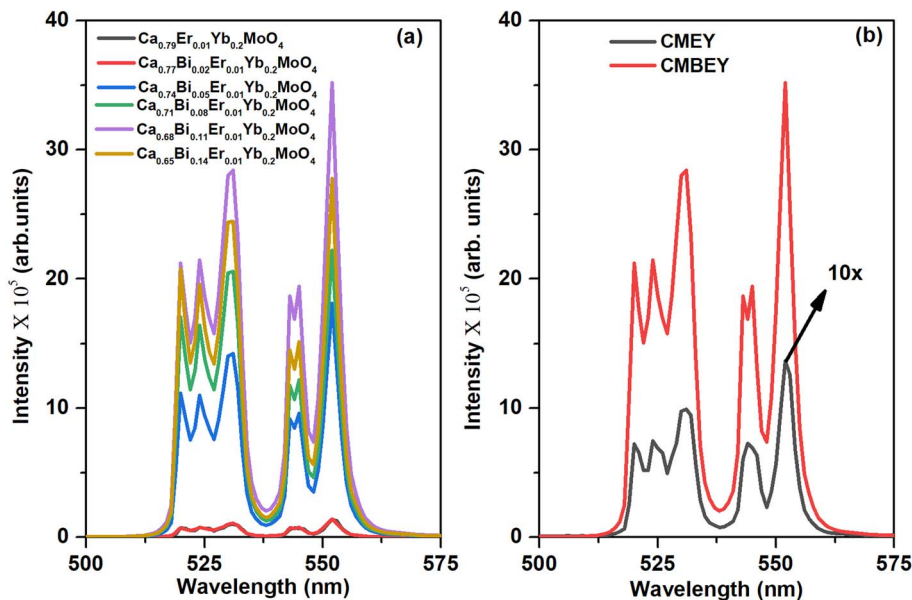
Fig. 5 (a) UC emission of powder samples of $Ca_{0.79-x}Bi_xEr_{0.01}Yb_{0.2}MoO_4$, with varying Bi concentrations ($x = 0.00$, 0.02, 0.05, 0.08, 0.11, and 0.14), (b) comparison of the UC emission spectra of CMEY and CMBEY samples both using 980 nm laser as excitation source.

the band gap. This leads to a decrease in the energy gap, which could explain the observed differences in energy band gap values.[48] According to the interpretations from XRD and SEM analyses, the presence of Bi^{3+} ions in the CMEY phosphors increases both the crystallite size and particle size. It is obvious that the bandgap decreases as the particle size increases.[49]

3.3.2 Upconversion spectra analysis. The UC spectra of the synthesised $Ca_{0.79-x}Bi_xEr_{0.01}Yb_{0.2}MoO_4$ ($x = 0.00$, 0.02, 0.05, 0.08, 0.11, and 0.14) phosphors are carried out using the 980 nm laser as an excitation source. Fig. 5(a) portrays the UC spectra of $Ca_{0.79-x}Bi_xEr_{0.01}Yb_{0.2}MoO_4$ sample. The concentration of Bi^{3+} was varied by (x) from 0.02 to 0.14, while that of Yb^{3+} and Er^{3+} was held fixed at 0.20 and 0.01, respectively. The UC luminescence spectra exhibited two robust emission bands located at 531 nm and 553 nm, respectively corresponding to $^2H_{11/2} \rightarrow {}^4I_{15/2}$ and $^4S_{3/2} \rightarrow {}^4I_{15/2}$ transitions of Er^{3+}.[10] The initial increase in the UC emission intensity occurred as the concentration of Bi^{3+} ions increases from $x = 0.02$ to 0.11, with a maximum value observed at $x = 0.11$. However, after surpassing the optimal concentration, the UC emission intensity of the $Ca_{0.79-x}Bi_x-Er_{0.01}Yb_{0.2}MoO_4$ sample is decreased due to the concentration quenching effect at higher concentrations.[10] Concentration quenching is a phenomenon in which the luminescence efficiency of a phosphor material decreases with increasing dopant concentration beyond certain limit. In the case of tri-doped phosphors like Bi^{3+}, Er^{3+}, and Yb^{3+} co-doped $CaMoO_4$, the concentration quenching can occur due to several reasons, including energy transfer processes, cross-relaxation, and self-absorption. In this case, Bi^{3+}, Er^{3+}, and Yb^{3+} are ions with different energy levels. Yb^{3+} is typically used as a sensitizer ion, that absorbs excitation photons and transfers the energy to other ions, such as Er^{3+}, which then emit photons at different wavelengths. However, when the concentration of these ions is

increased, energy transfer processes become less efficient, resulting in decreased luminescence efficiency. Additionally, cross-relaxation can occur between the dopant ions at high concentrations. In this process, excited dopant ions transfer their energy to neighbouring dopant ions, resulting in non-radiative energy losses and reduced luminescence. The energy transfer can also be limited by the distance between the dopant ions, and at high concentrations. The distance between the ions becomes too small, leading to an increase in energy transfer through cross-relaxation. Finally, self-absorption is another reason for concentration quenching. At high concentrations, the emission from the dopant ions can be absorbed by other dopant ions of the same type, reducing the luminescence efficiency. This is particularly relevant for materials with a narrow absorption or emission bandwidth.[41,50]

In conclusion, our study indicates that $Ca_{0.68}Bi_{0.11}Er_{0.01}-Yb_{0.2}MoO_4$ is the optimized sample among the series of Bi^{3+} co-doped Er^{3+}/Yb^{3+}: $CaMoO_4$ samples. Nonetheless, the UC emission peak intensity is subject to different factors, such as the excitation flux and the phosphor mass. For comparative purposes, we used the same instrumental parameters, including the excitation wavelength, slit width, and integration time, for both the CMEY and CMBEY samples. As shown in Fig. 5(b), the UC emission intensity for the CMBEY sample was nearly twenty-five times higher than that of the CMEY sample. The incorporation of Bi^{3+} ions enhances the luminescence intensity of the phosphors through various mechanisms. One possible mechanism is that Bi^{3+} ions can act as a sensitizer as well as the surface modifier,[40] facilitating the efficient energy transfer between Yb^{3+} and Er^{3+} ions. This improved energy transfer can lead to enhanced UC luminescence intensity. Additionally, the local site distortion caused by Bi^{3+} ions may modify the crystal field environment around the Er^{3+} ions,
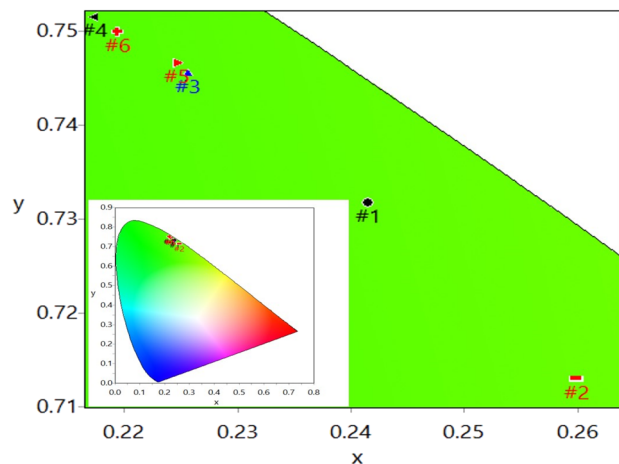
Fig. 6 Zoomed-in version of the CIE chromaticity diagram for the UC emission of $Ca_{0.79}Er_{0.01}Yb_{0.2}MoO_4$ (#1), $Ca_{0.77}Bi_{0.02}Er_{0.01}Yb_{0.2}MoO_4$ (#2), $Ca_{0.74}Bi_{0.05}Er_{0.01}Yb_{0.2}MoO_4$ (#3), $Ca_{0.71}Bi_{0.08}Er_{0.01}Yb_{0.2}MoO_4$ (#4), $Ca_{0.68}Bi_{0.11}Er_{0.01}Yb_{0.2}MoO_4$ (#5), and $Ca_{0.65}Bi_{0.14}Er_{0.01}Yb_{0.2}MoO_4$ (#6) phosphor samples under 980 nm laser excitation. The inset displays the CIE chromaticity diagram for all six samples without zooming.

potentially leading to more efficient radiative transitions and hence, an increase in luminescence intensity.[50]

3.3.3 Chromaticity coordinate analysis.
Fig. 6 displays the Commission International de I′ Eclairage (CIE) chromaticity diagram of all the six samples, namely $Ca_{0.79}Er_{0.01}Yb_{0.2}MoO_4$ (#1), $Ca_{0.77}Bi_{0.02}Er_{0.01}Yb_{0.2}MoO_4$ (#2), $Ca_{0.74}Bi_{0.05}Er_{0.01}Yb_{0.2}MoO_4$ (#3), $Ca_{0.71}Bi_{0.08}Er_{0.01}Yb_{0.2}MoO_4$ (#4), $Ca_{0.68}Bi_{0.11}Er_{0.01}Yb_{0.2}MoO_4$ (#5), and $Ca_{0.65}Bi_{0.14}Er_{0.01}Yb_{0.2}MoO_4$ (#6) for their UC emission using CIE 1931. The CIE coordinates of each sample are (0.2415, 0.7317), (0.2599, 0.7130), (0.2256, 0.7455), (0.2174, 0.7515), (0.2246, 0.7466), and (0.2194, 0.7499), respectively. The CIE coordinates of the synthesized $Ca_{0.79-x}Bi_xEr_{0.01}Yb_{0.2}MoO_4$ ($x = 0.00, 0.02, 0.05, 0.08, 0.11,$ and 0.14) showed little change in their CIE coordinates after Bi^{3+} doping. This indicates that the emission color of the samples remained pure and could be used in lighting applications with improved light emission. In other words, the Bi-doped samples exhibited stable and improved light emission with minimal alteration of their emission color, which is advantageous for their potential use.

3.4 Temperature dependent UC measurement: optical temperature sensing application

A temperature depended UC emission was monitored for CMEY and CMBEY samples. Initially, both the samples were calcined at 900 °C for the comparison. A 980 nm continuous wave laser source with a low power was used for excitation to prevent excessive heating from the source itself. The external temperature of the sample was regulated using a program given to homemade heater, and the UC emission spectra were observed in the temperature range from 298 K to 523 K for CMEY and 300 K to 598 K for CMBEY samples. The temperature-dependent multi-phonon non-radiative decay can be described by the equation

$$W_{NR}(T) = W_{NR}(0)(1 - e^{-h\nu/kT})^{-n} \qquad (5)$$

The equation used to describe the temperature-dependent multi-phonon non-radiative decay is characterized by $W_{NR}(T)$ and $W_{NR}(0)$, which represent the non-radiative decay rates at temperatures T and 0 K, respectively. The analysis of the temperature-dependent UC spectra was conducted because of the potential for population redistribution due to thermal excitation of the energy difference between the $^2H_{11/2}$ and $^4S_{3/2}$ states of the Er^{3+} ion. The fluorescence intensity ratio (FIR) was plotted against temperature and explained using Boltzmann's distribution, as described by eqn (6) and (7).

$$FIR = \frac{I_{531}(^2H_{11/2} \rightarrow {}^4I_{15/2})}{I_{553}(^4S_{3/2} \rightarrow {}^4I_{15/2})} = \frac{W_H g_H h\nu_H}{W_S g_S h\nu_S} \exp\left(\frac{-\Delta E}{k_B T}\right) \qquad (6)$$

$$FIR = B \exp\left(\frac{-\Delta E}{k_B T}\right) \qquad (7)$$

where, I_{531} and I_{553} are the integrated intensities for the transitions $^2H_{11/2} \rightarrow {}^4I_{15/2}$ ($\sim523-531$ nm) and $^4S_{3/2} \rightarrow {}^4I_{15/2}$ ($\sim544-553$ nm) bands of Er^{3+}-ion, respectively. g_H and g_S are the $(2J + 1)$ degeneracies of the levels $^2H_{11/2}$ and $^4S_{3/2}$. The variables W_H and W_S represent the probabilities of radiative transition, while $h\nu_H$ and $h\nu_S$ refer to the photon energies of the spontaneous emission transitions. ΔE represents the energy difference between the two emitting levels, k_B is the Boltzmann constant, and T represents the absolute temperature.

The energy bandgap between two thermally coupled levels, $^2H_{11/2}$ and $^4S_{3/2}$, can be calculated by taking the natural log of both sides of eqn (7). This yields the expression

$$\ln(FIR) = \ln(B) + \left(-\frac{\Delta E}{k_B T}\right) = \ln(B) + \left(-\frac{C}{T}\right) \qquad (8)$$

The determination of the unknown constants B and C is required, with the constant B being influenced by the properties of the prepared phosphor, such as degeneracy (g_H and g_S) and spontaneous emission probability (W_H and W_S), as well as the detection system's response. Fig. 7(a) and (d) displays the temperature-induced variations in the intensity of the UC emission peaks, located at 531 nm and 553 nm of the samples CMEY and CMBEY, respectively. The intensity of the 531 nm peak initially rises with increasing temperature until it reaches 398 K, then begins to decline beyond this temperature. This trend is also followed by 553 nm wavelength. Eqn (8) can be utilized to calculate the energy bandgap between two levels that are thermally coupled. This equation is based on the logarithm of the fluorescence intensity ratio (FIR), as well as the constants B and C, and the energy difference ΔE. The constants B and C are influenced by the properties of the prepared phosphor, including degeneracy and spontaneous emission probability, as well as the detection system's response.

Eqn (8) is plotted as a linear graph of ln(FIR) against $1/T$ as shown in Fig. 7(b) and (e), with the calculated slope and intercept being 506.56 ± 40.40, 1.91 ± 0.10 for CMEY and 688.834 ± 49.39, 2.365 ± 0.136 for CMBEY. This results in energy gaps of 352.19 cm^{-1} and 478.92 cm^{-1} for CMEY and CMBEY samples,
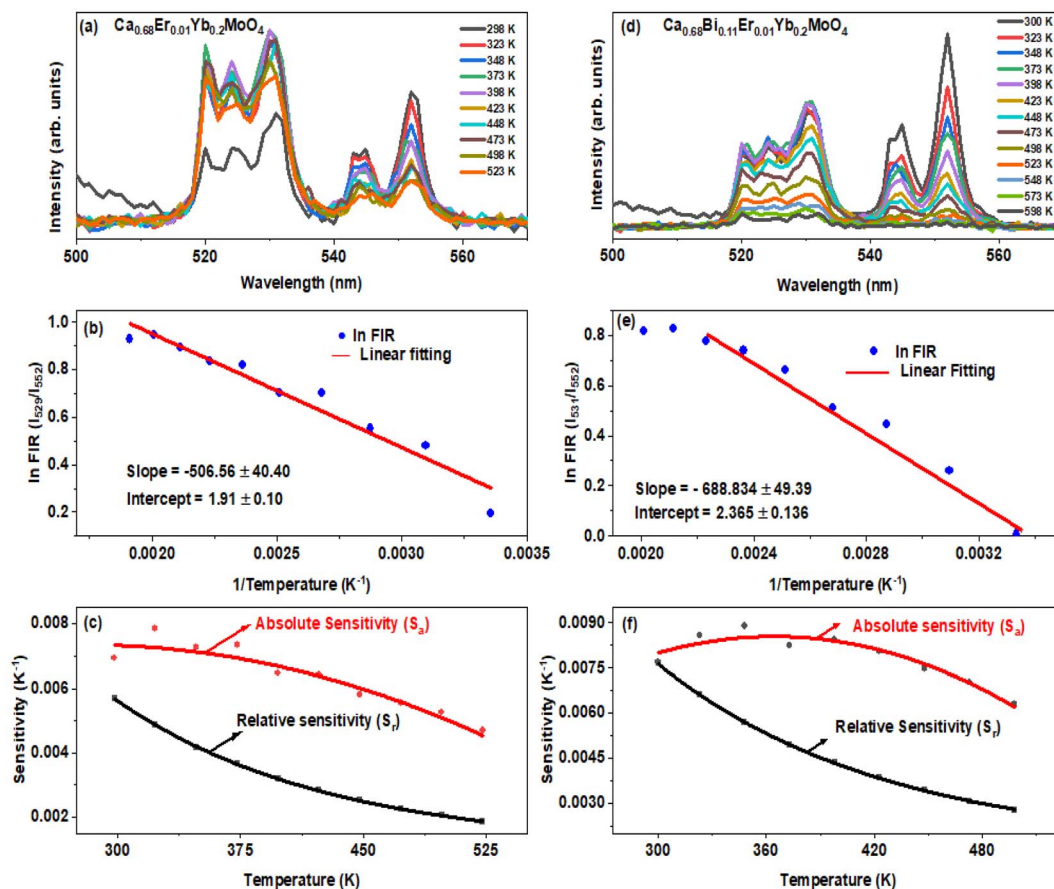
Fig. 7 Upconversion spectra of (a) $Ca_{0.68}Er_{0.01}Yb_{0.2}MoO_4$ and (d) $Ca_{0.68}Bi_{0.11}Er_{0.01}Yb_{0.2}MoO_4$ phosphor samples at different temperatures. The logarithm of the FIR as a function of the inverse temperature for (b) $Ca_{0.68}Er_{0.01}Yb_{0.2}MoO_4$, and (e) $Ca_{0.68}Bi_{0.11}Er_{0.01}Yb_{0.2}MoO_4$. The relative and absolute sensitivity for (c) $Ca_{0.68}Er_{0.01}Yb_{0.2}MoO_4$ and (f) $Ca_{0.68}Bi_{0.11}Er_{0.01}Yb_{0.2}MoO_4$ samples, respectively.

respectively.[10] To observe the thermal sensitivity of the prepared phosphors, the relative sensitivity (S_r) and absolute sensitivity (S_a) were also calculated. S_a is defined as the rate of change of FIR with temperature, while S_r is used to compare the sensitivity of different materials. The plots of S_a and S_r for both CMEY and CMBEY against increasing temperature are shown in Fig. 7(c) and (f), respectively. The absolute sensitivity for both samples initially increases, reaches a maximum value, and then decreases. The maximum relative sensitivity for CMEY is 0.0057 K^{-1} at 298 K and 0.0068 K^{-1} at 300 K for CMBEY. The maximum absolute sensitivities for CMEY and CMBEY are 0.00786 K^{-1} at 323 K and 0.0079 K^{-1} at 348 K, respectively, with CMBEY having higher sensitivity.

Local site distortions caused by Bi^{3+} doping improves the luminescence properties of the phosphors. The Bi^{3+} ions modify the local crystal field environment around the Er^{3+} and Yb^{3+} ions, which can enhance the luminescence intensity and improve the temperature sensing sensitivity of the phosphors. Hence Bi^{3+} ion doping into the $Ca_{0.79}Er_{0.01}Yb_{0.2}MoO_4$ phosphor enables the better temperature sensing capabilities. However, further investigation of the optical properties and temperature-dependent luminescence behaviour are necessary to fully understand the effect of Bi^{3+} co-doping on the $Ca_{0.79}Er_{0.01}Yb_{0.2}MoO_4$ phosphor.

4. Conclusion

In conclusion, this study has effectively demonstrated the significant impact of co-doping Bi^{3+} ions on luminescence enhancement of Er^{3+}/Yb^{3+} co-doped $CaMoO_4$ phosphor. Bi^{3+} co-doping creates a local distortion while the average tetragonal structure of $CaMoO_4$ remains intact. This creates asymmetry around the Er^{3+} ions (substituted at Ca^{2+} site) which improves the UC emission. Further, our calculations on XRD data show a reduction in dislocation density (72.80 × 10^{12} m^{-2} to 51.02 × 10^{12} m^{-2}) and micro-strain (16.8 × 10^{-4} to 15.8 × 10^{-4}) with the introduction of Bi in $Ca_{0.79}Er_{0.01}Yb_{0.2}MoO_4$ crystal structure, which also favours the enhancement of upconversion emission as it reduces the non-radiative channels. The overall enhancement of the UC emission by the combined effects is nearly 25-folds which improves relative sensitivity significantly. At 300 K, the relative sensitivity of the Bi^{3+} co-doped sample was found to be 0.0068 K^{-1}. Conversely, the sample without Bi co-doping had a relative sensitivity of 0.0057 K^{-1} at 298 K. These findings provide compelling evidence for the potential of Bi^{3+} co-doping to optimize the performance of Er^{3+}/Yb^{3+} co-doped $CaMoO_4$ as a temperature sensor in FIR based applications. Further, this study also constitutes a significant step forward in the

development of efficient and effective temperature sensing materials based on Bi^{3+} co-doping in lanthanide phosphors.

Conflicts of interest

There are no conflicts to declare.

Acknowledgements

References

1 S. A. Wade, S. F. Collins and G. W. Baxter, *J. Appl. Phys.*, 2003, **94**, 4743–4756.
2 V. K. Rai and S. B. Rai, *Appl. Phys. B*, 2007, **87**, 323–325.
3 S. K. Singh, K. Kumar and S. B. Rai, *Sens. Actuators, A*, 2009, **149**, 16–20.
4 J. Cao, X. Li, Z. Wang, Y. Wei, L. Chen and H. Guo, *Sens. Actuators, B*, 2016, **224**, 507–513.
5 J. Cao, W. Chen, D. Xu, F. Hu, L. Chen and H. Guo, *J. Lumin.*, 2018, **194**, 219–224.
6 P. Du, L. Luo, X. Huang and J. S. Yu, *J. Colloid Interface Sci.*, 2018, **514**, 172–181.
7 M. A. Hernández-Rodriguez, A. D. Lozano-Gorrín, V. Lavín, U. R. Rodríguez-Mendoza, I. R. Martín and F.-J. Manjón, *J. Lumin.*, 2018, **202**, 316–321.
8 A. K. Choudhary, S. K. Singh, A. Dwivedi, A. Bahadur and S. B. Rai, *Methods Appl. Fluoresc.*, 2018, **6**, 35014.
9 M. Sharma, P. Singh, S. K. Singh and P. Singh, *Opt. Mater.*, 2022, **133**, 112925.
10 S. Singh, S. Kachhap, A. K. Singh, S. Pattnaik and S. K. Singh, *Methods Appl. Fluoresc.*, 2022, **10**, 44004.
11 F. Wang, J. Wang and X. Liu, *Angew. Chem., Int. Ed.*, 2010, **49**, 7456–7460.
12 P. Huang, W. Zheng, S. Zhou, D. Tu, Z. Chen, H. Zhu, R. Li, E. Ma, M. Huang and X. Chen, *Angew. Chem.*, 2014, **126**, 1276–1281.
13 Q. Zou, P. Huang, W. Zheng, W. You, R. Li, D. Tu, J. Xu and X. Chen, *Nanoscale*, 2017, **9**, 6521–6528.
14 F. Wang and X. Liu, *Chem. Soc. Rev.*, 2009, **38**, 976–989.
15 F. Wang, Y. Han, C. S. Lim, Y. Lu, J. Wang, J. Xu, H. Chen, C. Zhang, M. Hong and X. Liu, *Nature*, 2010, **463**, 1061–1065.
16 F. Wang, R. Deng, J. Wang, Q. Wang, Y. Han, H. Zhu, X. Chen and X. Liu, *Nat. Mater.*, 2011, **10**, 968–973.
17 F. Wang, X. Xue and X. Liu, *Angew. Chem.*, 2008, **120**, 920–923.
18 C.-K. Duan, M. Yin, K. Yan and M. F. Reid, *J. Alloys Compd.*, 2000, **303**, 371–375.
19 D. Hreniak, J. Hölsä, M. Lastusaari and W. Stręk, *J. Lumin.*, 2007, **122**, 91–94.
20 L. Marciniak, M. Stefanski, R. Tomala, D. Hreniak and W. Strek, *Opt. Mater.*, 2015, **41**, 17–20.
21 Y. Chen, W. He, H. Wang, X. Hao, Y. Jiao, J. Lu and S. Yang, *J. Lumin.*, 2012, **132**, 2404–2408.
22 L. Marciniak, D. Hreniak, A. Dobrowolska and E. Zych, *Appl. Phys. A*, 2010, **99**, 871–877.
23 Y. Liu, W. Luo, H. Zhu and X. Chen, *J. Lumin.*, 2011, **131**, 415–422.
24 W. Luo, Y. Liu and X. Chen, *Sci. China Mater.*, 2015, **58**, 819–850.
25 G. Xiang, X. Liu, Q. Xia, X. Liu, S. Xu, S. Jiang, X. Zhou, L. Li, D. Wu and L. Ma, *Talanta*, 2021, **224**, 121832.
26 G. Chen, H. Liu, H. Liang, G. Somesfalean and Z. Zhang, *J. Phys. Chem. C*, 2008, **112**, 12030–12036.
27 Q. Cheng, J. Sui and W. Cai, *Nanoscale*, 2012, **4**, 779–784.
28 W. You, D. Tu, W. Zheng, P. Huang and X. Chen, *J. Lumin.*, 2018, **201**, 255–264.
29 I. Mayer and S. Cohen, *J. Solid State Chem.*, 1983, **48**, 17–20.
30 S.-D. Liu, L.-L. Dong, Y. Xu, X. Zhang, T.-Q. Ren, X.-D. Xu, Y.-D. Peng, Y.-P. Zhang, H.-Y. Zhang and D.-H. Li, *Appl. Opt.*, 2016, **55**, 7659–7662.
31 H. Ji, Z. Huang, Z. Xia, M. S. Molokeev, X. Jiang, Z. Lin and V. V Atuchin, *Dalton Trans.*, 2015, **44**, 7679–7686.
32 H. J. Seo, *J. Alloys Compd.*, 2014, **604**, 100–105.
33 M. D. Wisser, S. Fischer, P. C. Maurer, N. D. Bronstein, S. Chu, A. P. Alivisatos, A. Salleo and J. A. Dionne, *ACS Photonics*, 2016, **3**, 1523–1530.
34 Y. Zhu, Y. Liu, M. G. Brik, L. Huang, T. Xuan and J. Wang, *Opt. Mater.*, 2017, **74**, 52–57.
35 Y. Wang, X. Wang, Y. Mao and J. A. Dorman, *J. Phys. Chem. C*, 2022, **126**, 11715–11722.
36 L. Zhang and X. Sun, *J. Mater. Sci.: Mater. Electron.*, 2020, **31**, 9160–9166.
37 W. Wang, S. Song, B. Cao and J. Li, *J. Lumin.*, 2022, **247**, 118901.
38 H. Hu, C. Deng, J. Xu, K. Zhang and M. Sun, *J. Exp. Nanosci.*, 2015, **10**, 1336–1346.
39 R. S. Yadav, A. Rai and S. B. Rai, *Sci. Rep.*, 2021, **11**, 4148.
40 R. S. Yadav, D. Kumar, A. K. Singh, E. Rai and S. B. Rai, *RSC Adv.*, 2018, **8**, 34699–34711.
41 J. Kong, J. Liu, F. Marlton, M. R. V. Jørgensen and A. Pramanick, *Phys. Rev. B*, 2021, **103**(18), 184104.
42 S. P. S. Porto and J. F. Scott, *Phys. Rev.*, 1967, **157**, 716.
43 J. C. Sczancoski, L. S. Cavalcante, M. R. Joya, J. A. Varela, P. S. Pizani and E. Longo, *Chem. Eng. J.*, 2008, **140**, 632–637.
44 A. K. Parchur and R. S. Ningthoujam, *Dalton Trans.*, 2011, **40**, 7590–7594.
45 S. Dutta, S. Som and S. K. Sharma, *RSC Adv.*, 2015, **5**, 7380–7387.
46 Z. Xianju, Y. Xiaodong, X. Tengjiao, Z. Kaining, C. Tianyu, Y. A. N. Hao and W. Zhongqing, *J. Rare Earths*, 2013, **31**, 655–659.
47 S. Vidya, S. Solomon and J. K. Thomas, *Phys. Status Solidi*, 2012, **209**, 1067–1074.
48 K. Saidi, W. Chaabani and M. Dammak, *RSC Adv.*, 2021, **11**, 30926–30936.
49 P. Nayak, S. S. Nanda and S. Dasha, in *AIP Conference Proceedings*, AIP Publishing LLC, 2020, vol. 2265, p. 30070.
50 M. Yang, Y. Sui, S. Wang, X. Wang, Y. Wang, S. Lü, Z. Zhang, Z. Liu, T. Lü and W. Liu, *J. Alloys Compd.*, 2011, **509**, 827–830.